Chem

CellPress

Article

# Construction of a three-state responsive framework from a bistable photoswitch

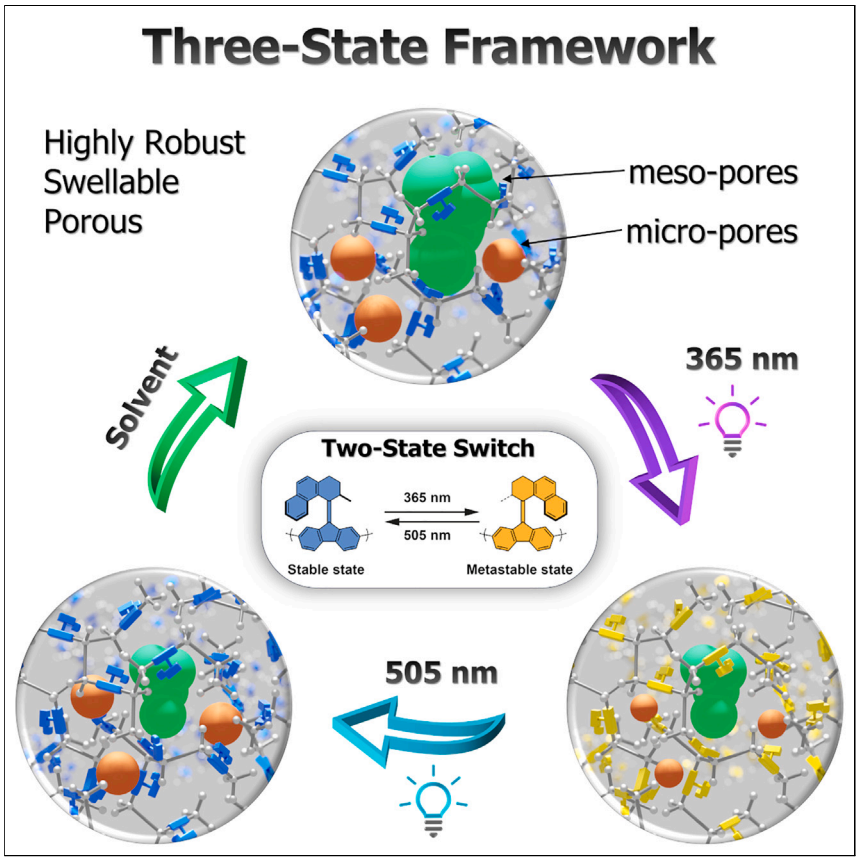


The integration of molecular photoswitches into porous structures enables fabrication of materials capable of interconversion between two states inherently linked to the appended molecules. Here, we showcase a flexible porous aromatic framework constructed exclusively from a bistable overcrowded alkene-derived molecular photoswitch. The interplay between the framework's flexibility, hierarchical porosity, and geometrical changes associated with the isomerization of the photoswitch results in three distinct porosity states that can be sequentially interconverted upon the application of physical and chemical stimuli.

Jinyu Sheng, Jacopo Perego, Wojciech Danowski, ..., Piero Sozzani, Angiolina Comotti, Ben L. Feringa

danowski@unistra.fr (W.D.)
silvia.bracco@unimib.it (S.B.)
angiolina.comotti@unimib.it (A.C.)
b.l.feringa@rug.nl (B.L.F.)

## Highlights

Swellable and photoresponsive solid porous aromatic frameworks are fabricated

Toggling between three porosity states by a two-state photoswitch

Fully reversible light-induced solid-state photoisomerization in the bulk

Sheng et al., Chem 9, 2701–2716
September 14, 2023 
https://doi.org/10.1016/j.chempr.2023.08.004

Chem

CellPress

Article

# Construction of a three-state responsive framework from a bistable photoswitch

Jinyu Sheng,[1,6] Jacopo Perego,[2,6] Wojciech Danowski,[1,3,*] Silvia Bracco,[2,*] Shaoyu Chen,[1,4] Xiaotian Zhu,[1] Charl X. Bezuidenhout,[2] Simon Krause,[1,5] Wesley R. Browne,[1] Piero Sozzani,[2] Angiolina Comotti,[2,*] and Ben L. Feringa[1,7,*]

## SUMMARY

**The integration of photoswitchable elements into porous solids provides fascinating opportunities to modulate material properties. However, the fabrication strategies of these materials are dedicated only to preserving the function of the photoswitches in the solid while introducing new properties beyond those offered by the individual components remains challenging. Here, we present a three-state porous aromatic framework constructed from a bistable overcrowded alkene-based photoswitch. The framework was fabricated using a Yamamoto coupling polymerization of an engineered hexadentate monomer to yield swellable and hierarchical microporous/mesoporous architectures with densely integrated photoswitches. The interplay of hierarchical porosity, flexible backbone, and reversible photoisomerization between two isomers generates three unique and distinct porosity states that can be accessed in sequence upon application of external stimuli to induce sponge-like behavior. This material represents a major step toward light-responsive materials capable of harnessing limited molecular-scale motion and converting it into an on-demand response over hierarchical length scales toward a practical output.**

## INTRODUCTION

Dynamic porous materials exploit the flexibility of the individual components or the entire network to give rise to adaptive and responsive structures.[1–13] Although various degrees of internal dynamics ranging from incoherent rotations[8,14,15] to geared motion[13,16] of the building blocks are ubiquitous to any structure possessing sufficient internal free volume, more complex and controllable structural deformations are required for practical applications.[17–20] Beyond this uncontrolled dynamic behavior, the integration of light-responsive artificial molecular switches[21,22] or machines[4,5,23–28] in porous frameworks[7,29–34] allows us to harness their nanoscopic motion and translate it on demand in a non-invasive manner into the consistent and predictable change in the material performance under a wide range of external conditions. The fabrication of light-responsive porous materials allows significant advantages by alleviating the geometrical constraints associated with photoisomerization, although providing sufficient flexibility or free volume to accommodate the structural changes. Pioneering studies on azobenzenes, dithienylethenes, spiropyrans, stilbenes, and overcrowded alkenes (OAs) incorporated in metal-organic frameworks (MOFs),[35–37] covalent-organic frameworks (COFs),[38–41] and porous aromatic frameworks (PAFs)[42,43] proved the feasibility and showed opportunities offered by this approach, demonstrating modulation of a wide range of properties,

## THE BIGGER PICTURE

Incorporation of molecular photoswitches in porous materials offers opportunities to gain remote control of their gas uptake and release properties. These materials are typically designed to facilitate isomerization in the solid by minimizing the interactions between the embedded switches and scaffold and consequently operate by switching between the two inherent states of the responsive components. Here, we demonstrate a porous and flexible aromatic framework constructed exclusively from the overcrowded alkene-derived bistable molecular photoswitch. The interplay between framework flexibility, hierarchical porosity, and geometrical changes associated with the photoisomerization enabled reversible interconversion of the framework between three porosity states orchestrated by the photoswitch. These results demonstrate that integration of molecular photoswitches in solid porous materials can lead to new functions beyond those associated with isolated molecules in solution.

such as gas uptake, conductivity, or guest-molecule separation, by isomerization of light-responsive units integrated in the framework.[44–58] In addition, several strategies circumventing the limited light-penetration depth in these materials were developed yielding systems that undergo facile photoisomerization in isolated crystals, films, and even in bulk materials.[30,48,51,56,59] However, photochemical isomerization in these systems is mostly restricted to the individual responsive units, which remain independent and reciprocally unaffected; thus, the stimulus is not further propagated. Consequently, the functionality of the entire system and the perspectives of the materials as actuators were limited. In contrast, the insertion of active elements in each monomer unit of a 3D network allows the incorporation of multiple dynamic elements, which could potentially open more accessible states or lead to the properties beyond those offered by individual elements. Therefore, we envisioned that the monomers displaying intrinsic responsiveness due to the light-driven isomerization between two distinct configurations, once polymerized, would transmit their stimulated change through the constraints to the overall network. Here, we present the synthesis of a monomer functionalized with a photoswitch in its core and two lateral wings to yield a highly porous switchable framework (PSF) (Figures 1A and 1B) collectively responsive to light and capable of switching between three distinct porosity states orchestrated by the bistable OA-derived photoswitching monomer units. The designed monomer comprises both the OA photoswitch and reactive hexabromine functionalized groups that serve as responsive and porogen units (Figure 1B). The amphifunctional structure of the monomer ensures the desired connectivity in the framework and precludes the formation of phase-separated regions or blocks of switch and porogen, producing a micropore and a mesopore architecture (state I, Figure 1C). Indeed, we could attain the fully reversible bulk photoswitching from the stable to the metastable diastereomer and back to the stable diastereomer using two distinct wavelengths of light, despite high concentration of molecular switches embedded in the material. The facile back optical switching was demonstrated for the first time in PAFs, establishing a benchmark for the generation of a fully light-controlled PSF materials. The nanoscopic isomerization process in the solid state induced by irradiation at $\lambda$ = 365 nm leads to a contractile sponge-like behavior and drives the decrease of gas uptake of both mesopores and micropores (state II, Figure 1C). Subsequently, irradiation with green light ($\lambda$ = 505 nm) induces a photo-reversible expansion of the micropores (state III, Figure 1C), whereas the mesoporous region could be entirely regenerated by swelling the framework in a solvent and subsequent activation, thus regenerating pristine material (state I, Figure 1C). The PSF material acts as a mechanized nano-sponge switching between three distinct states arising from interactions of the bistable switch with the highly robust yet flexible architecture that provides sufficient free volume around the photoswitches to allow for unhindered movement in the solid state. The present system features various aspects of novelty: (1) one switch moiety between two porogenic units that ensures well-defined connectivity, topology, and stoichiometry (Figure 1A, top), in contrast to framework materials with a broad range of connectivities, topologies, and defectiveness (Figure 1A, bottom); (2) the framework architecture is further translated in the distinctly different properties showing remarkable swelling being a basis for the fully reversible nanosponge-like behavior; and (3) in addition to the microporosity, large hysteresis in the adsorption isotherms associated with the mesoporosity, which along with the green-light responsivity of the photoswitch embedded in the framework, form the basis for the unique feature of reversible control of three distinct porous states due to the cooperativity between switch and flexible framework. These findings indicate that the nanoscopic isomerization of the photoswitch units involves not just the core but also induces the conformational change of the lateral moieties, triggering the

[1]Stratingh Institute for Chemistry, University of Groningen, Nijenborgh 4, 9747 AG Groningen, the Netherlands

[2]Department of Materials Science, University of Milano Bicocca, Via R. Cozzi 55, Milan 20125, Italy

[3]University of Strasbourg, CNRS, ISIS UMR 7006, 8 allée Gaspard Monge, 67000 Strasbourg, France

[4]School of Fashion and Textiles, The Hong Kong Polytechnic University, Hong Kong, China

[5]Max Planck Institute for Solid State Research, Heisenbergstr. 1, 70569 Stuttgart, Germany

[6]These authors contributed equally

[7]Lead contact

*Correspondence: danowski@unistra.fr (W.D.), silvia.bracco@unimib.it (S.B.), angiolina.comotti@unimib.it (A.C.), b.l.feringa@rug.nl (B.L.F.)

https://doi.org/10.1016/j.chempr.2023.08.004

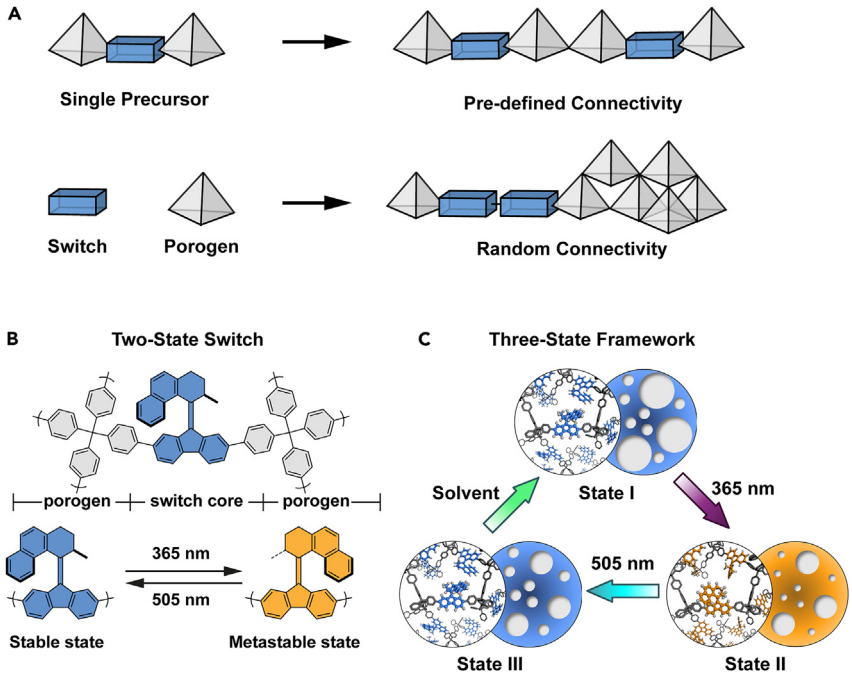


**Figure 1. Schematic depiction of the material design and interconversion between three porosity states**

(A) Schematic representation of two approaches for the construction of responsive PSFs.

(B) Molecular design of the multi-branch bistable switch and photoisomerization of the overcrowded alkene core in the porous material between two states triggered by irradiation at 365 and 505 nm.

(C) Schematic representation of the three distinct states of the framework material controlled reversibly by light and solvent. The micropore and mesopore in the framework can be contracted by irradiation at 365 nm. Regeneration of micropores can be achieved through irradiation with 505 nm light and of mesopores by solvent-assisted regeneration of the mesopores in the framework to the initial state.

rearrangement of the flexible framework and leading to the control of nano-sponge properties.

## RESULTS AND DISCUSSION

A hexabrominated monomer **1** featuring an OA core (Figure 2A) was designed as a precursor with well-defined topology and containing one switch moiety between two porogenic lateral units, both to generate a highly porous homogeneous aromatic framework and achieve a high concentration of photoswitch in the resulting 3D polymer. In contrast to OA-derived molecular motors, monomers **1** and **2** feature an expanded 6-membered ring upper part that pushes the naphthyl moiety closer to the fluorene stator, thereby increasing the steric interactions in the molecule to the point of practical suppression of the unidirectional rotation and thermal isomerization. Consequently, **1** and **2** operate as P-type bistable photoswitches, reversibly switching between stable and metastable diastereomers, with the latter being stable for several years at ambient temperatures, thereby constituting ideal candidates for the construction of light-addressable materials. Here, we envisioned that the highly branched architecture would allow homocoupling of the monomers into the PAF without the need for additional porogenic units that in turn would maximize the performance of the material upon light-induced isomerization of the responsive alkenes. In contrast to statistical co-polymerization of different monomers (Figure 1A

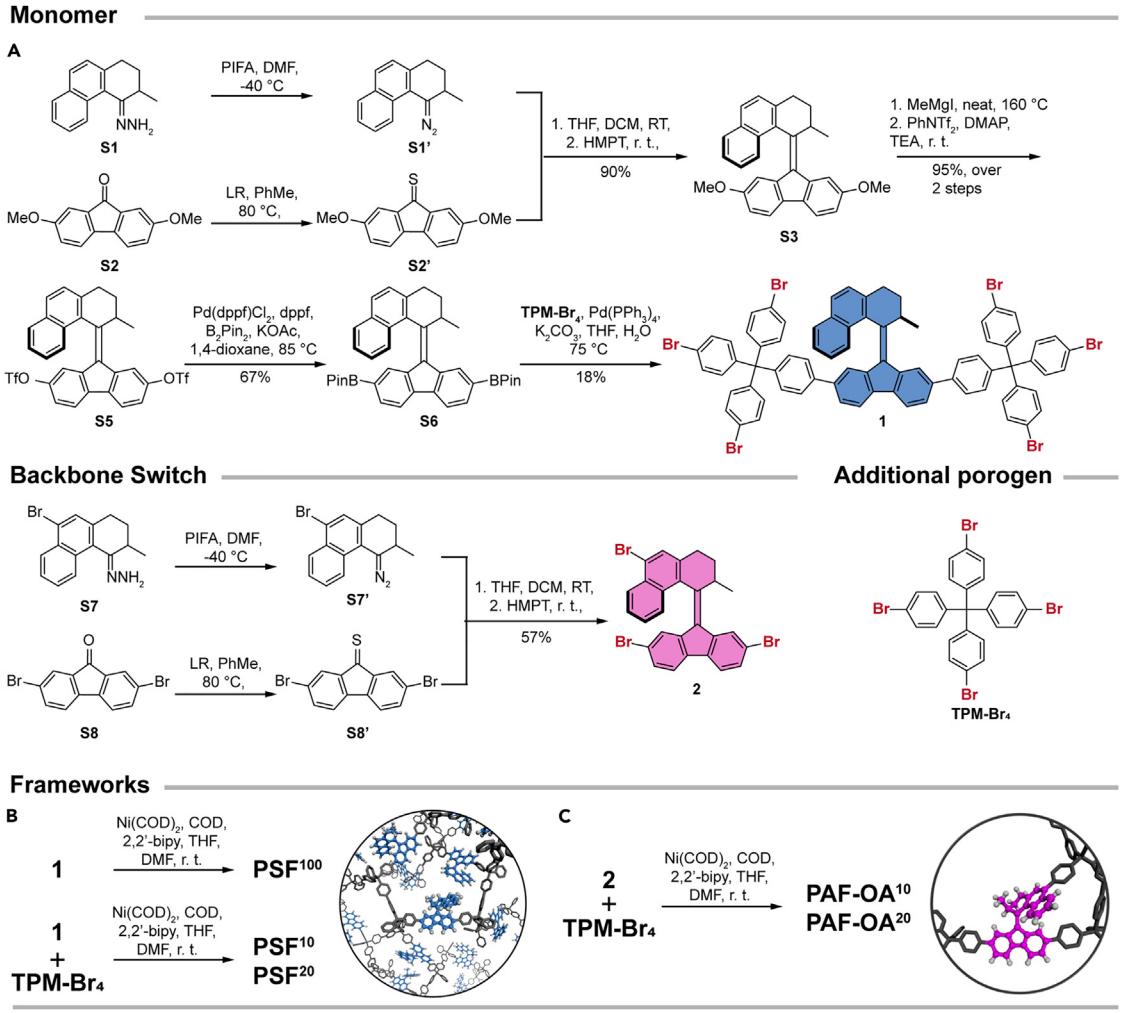


**Figure 2. Synthesis of the building blocks and fabrication of the materials**

(A) Synthesis of the multi-branch bistable switches **1** and **2** and structure of **TPM-Br$_4$**.

(B and C) Synthesis of **PSFs** by Yamamoto homo- and hetero-coupling reactions.

bottom), homocoupling of a single precursor (Figure 1A top) ensures the desired and pre-designed connectivity yielding a framework with a precise topology and therefore a specific property. The OA core **S3** was prepared (Figure 2A) by an improved Barton-Kellogg olefination,[60] which enabled large-scale synthesis (1.3 g, 3 mmol) with excellent yield (90% yield, see supplemental information for details). The key to the improved synthesis was the utilization of electron-donating methoxy substituents in the 2,7-position of the fluorenone **S2** that rendered the thioketone **S2′** much more stable in comparison with the dibrominated analog **S8′** and facilitated scale-up of the olefination in high yield. Subsequently, the designed building block **1** was prepared in four additional steps involving deprotection and a series of consecutive palladium-catalyzed reactions (see supplemental information for details and characterization of new compounds) with excellent yields.

Finally, OA-containing monomer **1** was polymerized into the homogeneous porous switchable framework (PSF$^{100}$) with controlled connectivity and topology using a Yamamoto homocoupling reaction (Figure 2B), and the solid material was dried and activated at 85°C under a dynamic vacuum prior to further characterization. In

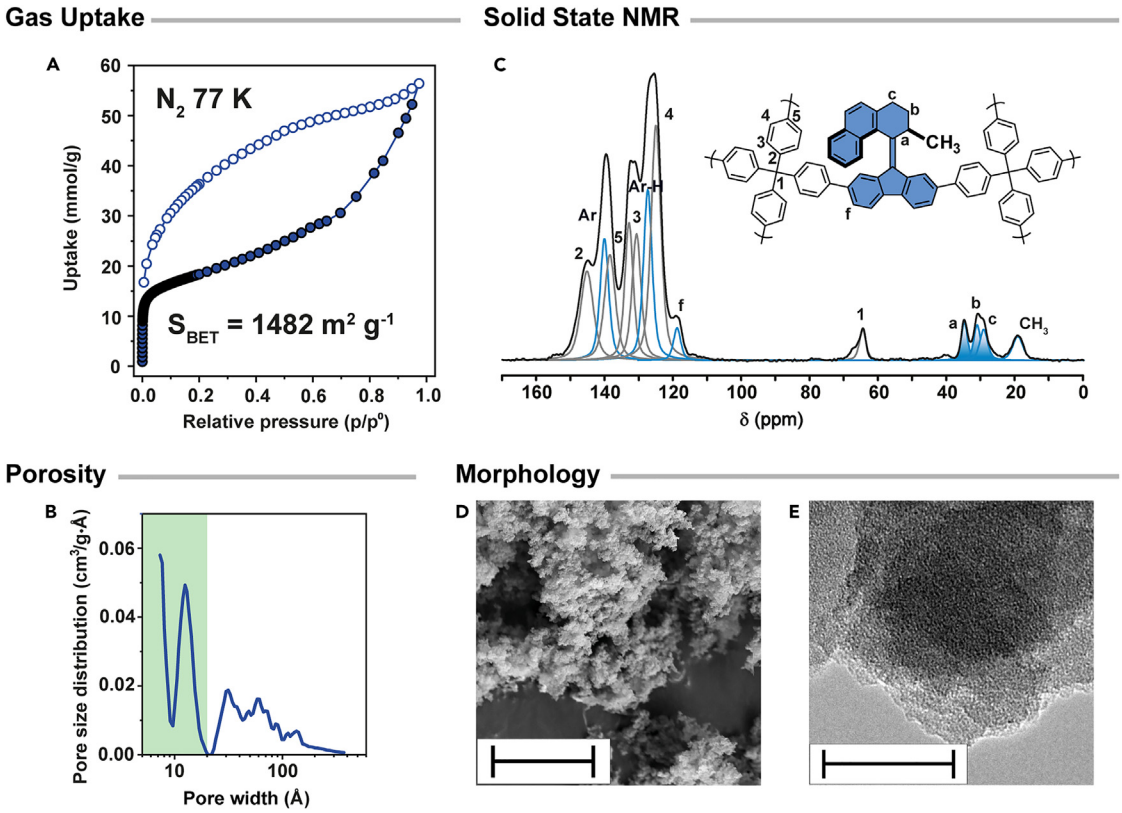


**Figure 3. Material characterization**

(A) Nitrogen adsorption isotherm of PSF$^{100}$ collected at 77 K. Surface areas as high as 1,679 and 1,482 $m^2/g$ were calculated according to Langmuir and BET models, respectively.

(B) Pore size distribution calculated according to NLDFT theory and carbon slit pore model. The micropore region (pore size below 20 Å) is highlighted in light green.

(C) $^{13}C\{^1H\}$ CP-MAS solid-state NMR of PSF$^{100}$ collected with a contact time of 2 ms and magic angle spinning of 12.5 kHz. The spectrum was simulated by Lorentzian line-shape functions.

(D) SEM image of PSF$^{100}$ nanoparticles (scale bars, 5 μm).

(E) TEM image of PSF$^{100}$ nanoparticles (scale bars, 50 nm).

addition, two co-monomeric PSF materials were synthesized by hetero-coupling reaction of tetrakis(4-bromophenyl)methane (TPM-$Br_4$) and **1** in two different ratios (≈10% and 20% mole fraction of **1**) to yield PSF$^{10}$ and PSF$^{20}$, respectively, to verify the impact of the switch loading on the porosity and the magnitude of the light-induced changes in porosity (Figure 2B; synthetic details and activation procedures are reported in the supplemental information section procedures for synthesis of building blocks and materials). Furthermore, frameworks containing tribrominated OA **2** (Figure 2A) incorporated in the backbone of the framework denoted as PAF-OA (≈10% and 20% mole fraction of **2** PAF-OA$^{10}$ and PAF-OA$^{20}$, respectively) were prepared as controls to access for the difference in dynamics between backbone and pendant incorporation of the photoswitch (Figure 2C).

The remarkable homogeneous framework PSF$^{100}$ exhibits Langmuir and Brunauer-Emmett-Teller (BET) surface areas as high as 1,679 and 1,482 $m^2\ g^{-1}$, respectively, and a large specific total pore volume of 1.88 $cm^3\ g^{-1}$, as determined by the $N_2$ sorption isotherms at 77 K (Figure 3A). The PSF$^{100}$ framework reveals a bimodal pore size distribution as calculated by non-local density functional theory (NLDFT),

comprising both microporosity and mesoporosity that highlight a hierarchical architecture (Figure 3B), further supported by *t-plot* analysis (Table S7; supplemental information section analysis of adsorption data: BET, Rouquerol, Langmuir plots and t-plot analysis). The large hysteresis that closes only at low partial pressures indicates a sponge-like behavior, in which the architecture may swell due to favorable interactions with the adsorbate and increase the mesopore capacity. Indeed, exposure of the activated $PSF^{20}$ to tetrahydrofuran (THF) led to substantial expansion of the material (40% relative linear expansion in the glass tube), indicating high flexibility of the material (Figure S4). Noteworthily, $N_2$ sorption isotherms collected at 77 K with prolonged equilibration times (up to 20 s, Figure S3) revealed the same hysteretic loops, indicating that the phenomenon is not associated with kinetic effects but with the mesoporosity of the framework. Similarly, large adsorption-desorption hysteresis loops have been observed in swellable PAF-type materials.[42,61] Elemental analysis indicated nearly complete removal of the bromine atoms from the sample, which is typical for the PAF-type materials fabricated by Yamamoto cross-coupling reaction owing to the acidic work-up of the product (see Table S3).[42,62] Nevertheless, the geometrical constraints imposed by the bent photoswitch core likely prevent a quantitative conversion of the bromides to the cross-coupled product. Instead, defects are formed by proton-termination of triphenylmethane moieties that may account for the observed large mesoporosity of the material.[61] Somewhat larger surface areas were produced under the same conditions by co-condensation of **1** with TPM-$Br_4$ monomer: $PSF^{10}$ and $PSF^{20}$ (Figure S6) display BET surface areas as high as 2,260 and 2,040 $m^2\ g^{-1}$ and pore volumes of 2.10 and 2.15 $cm^3\ g^{-1}$ indicating that increasing the monomer **1** fraction does not dramatically reduce the framework porosity (Figures S1 and S2). Noteworthily, the similar shape of $N_2$ adsorption isotherms at 77 K along the expected variations in the BET surface areas for all the synthesized PSFs indicates that the fabrication procedure yields materials with predictable and reproducible properties. Considering that the naphthyl moieties of the switch are expected to occupy a substantial part of the potential free volume, our successful fabrication strategy of highly porous and densely functionalized frameworks, encompassing monomers designed to form precisely defined branched networks, represents a major advance in the field of light-responsive porous materials. $^{13}C$ cross polarization (CP)-magic angle spinning (MAS) pointed out the connectivity of monomer units and the purity of the samples, proving the effective insertion of the desired molecular species (Figures 3C, S5, and S6). The stability of the $PSF^{100}$ material was verified by thermogravimetric analysis (TGA) that indicated high thermal stability with no decomposition over 500°C (Figure S7). Powder X-ray diffraction (PXRD) showed the amorphous nature of the frameworks (Figure S8), as expected for a material constructed by an irreversible reaction. Although the Yamamoto reaction may lead to a certain amount of short-range order and rigidity in pure PAFs (see Figure S5), the substantial lack of internal order in our materials induces a beneficial degree of swellability and flexibility to the framework, as testified by the large hysteresis loop, and promotes a large response upon switch isomerization. The scanning electron microscopy (SEM) and transmission electron microscopy (TEM) revealed that the PSFs materials are composed of small spherical nanoparticles of about 20–30 nm (Figures 3D, 3E, S9, and S10).

## Photochemical isomerization of the monomer

Monomer **1** undergoes a photochemical isomerization upon irradiation at 365 nm from the stable to metastable diastereomer and reverts to the stable diastereomer upon irradiation at 455 nm (Figure 4A). The switching core geometries for both the stable and metastable structures were optimized by density functional theory (DFT) on the B3LYP/6-31+G(d,p) level of theory. The double bond twisting angles

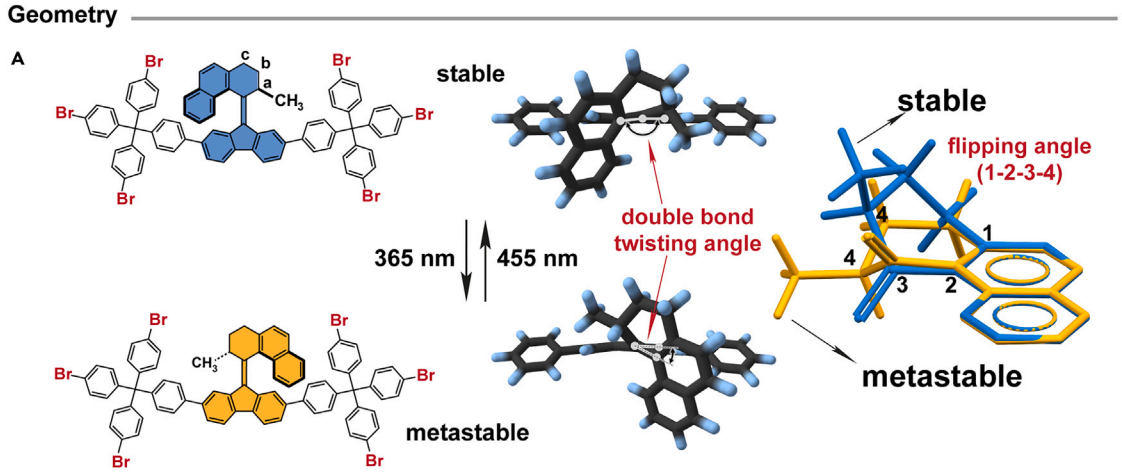
Geometry
A
stable
365 nm
455 nm
metastable
double bond
twisting angle
flipping angle
(1-2-3-4)
stable
metastable

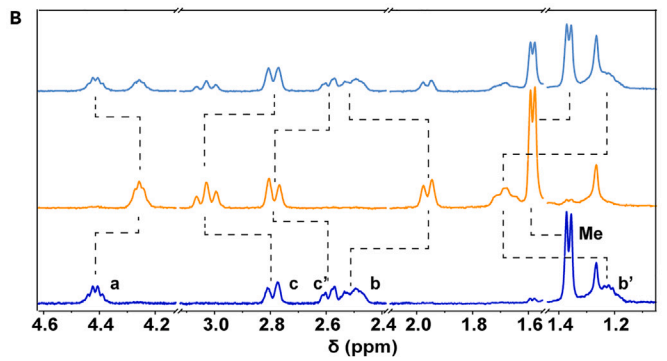
NMR Spectra
B
Me
a
c
c'
b
b'
δ (ppm)

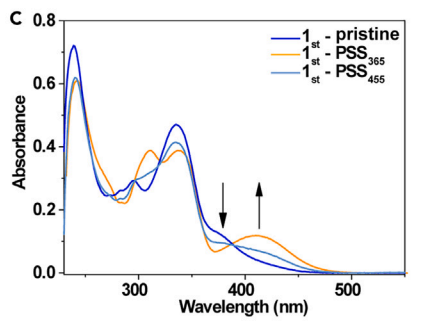
UV/Vis Spectra
C
1st - pristine
1st - PSS365
1st - PSS455
Absorbance
Wavelength (nm)

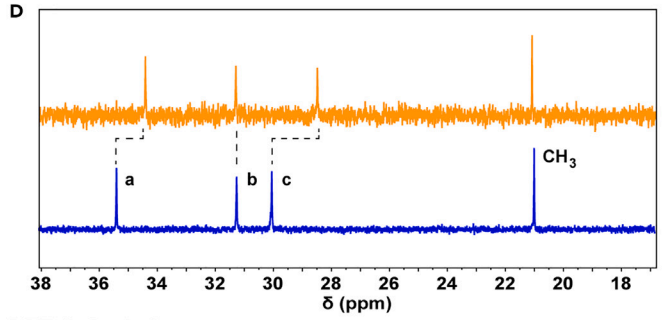
D
CH3
a
b
c
δ (ppm)

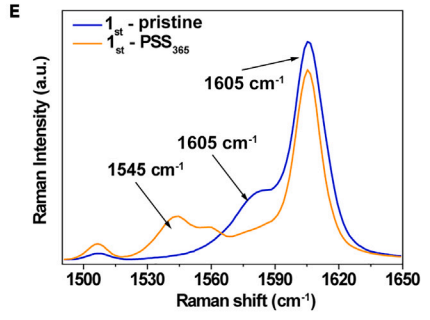
Raman Spectra
E
1st - pristine
1st - PSS365
1605 cm-1
1605 cm-1
1545 cm-1
Raman Intensity (a.u.)
Raman shift (cm-1)

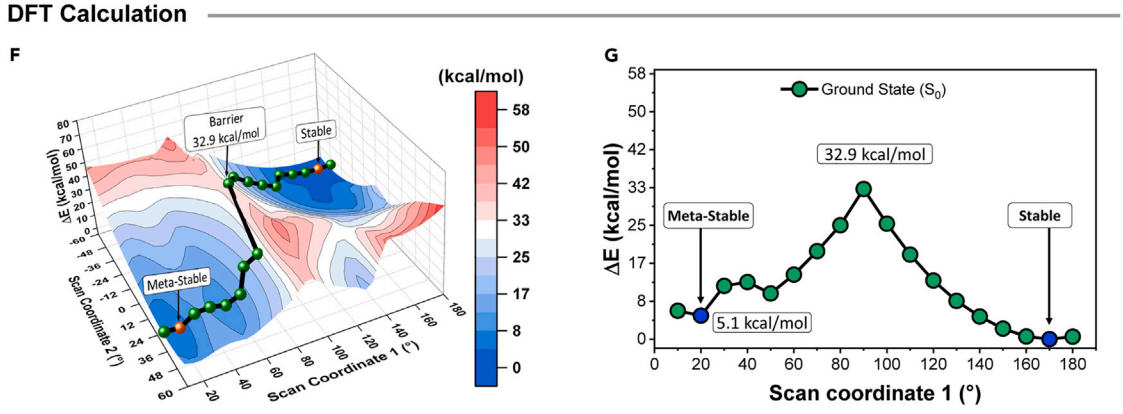
DFT Calculation
F
(kcal/mol)
Barrier
32.9 kcal/mol
Stable
Meta-Stable
ΔE (kcalmol)
Scan Coordinate 2 (°)
Scan Coordinate 1 (°)
G
Ground State (S0)
32.9 kcal/mol
Meta-Stable
Stable
5.1 kcal/mol
ΔE (kcal/mol)
Scan coordinate 1 (°)

**Figure 4. Photoisomerization in the solution**

(A) Schematic representation of the structural changes upon photoisomerization of the bistable switch **1** ($\mathbf{1}_{st} \leftrightarrow \mathbf{1}_{mst}$) (left panel) and DFT optimized geometries of the switching core calculated using the B3LYP/6-31+G(d,p) level of theory of both diastereomers (right panel).

(B) Comparison of the aliphatic part of the $^{1}$H NMR ($CD_2Cl_2$, 400 MHz, room temperature [RT]) spectra of $\mathbf{1}_{st}$ (blue spectrum) upon irradiation at 365 nm (orange spectrum) and concomitant irradiation at 455 nm (light blue, see A for the assignment of the resonances).

(C) Changes in the UV-vis electronic absorption spectra (DCM, 20 μM) of $\mathbf{1}_{st}$ (blue spectrum, $\mathbf{1}_{st}$-pristine) upon irradiation at 365 nm (orange spectrum, $\mathbf{1}_{st}$-$PSS_{365}$) and subsequent irradiation at 455 nm (light blue, $\mathbf{1}_{st}$-$PSS_{455}$).

(D) The comparison of the aliphatic part of the $^{13}$C NMR spectra ($CD_2Cl_2$, 400 MHz, RT) of the $\mathbf{1}_{st}$ (blue spectra) and $\mathbf{1}_{mst}$ (spectrum of the photostationary state obtained upon irradiation at 365 nm, orange spectra).

(E) Comparison of the Raman spectra (785 nm laser) of $\mathbf{1}_{st}$ (blue spectrum, $\mathbf{1}_{st}$-pristine) and $\mathbf{1}_{mst}$ (orange spectrum, $\mathbf{1}_{mst}$-$PSS_{365}$). Spectra were obtained by drop-casting pristine and irradiated solutions (DCM) onto a quartz substrate.

(F) 2D PES scan shown as a surface plot. Blue indicates low energy, and red indicates high energy. The minimum energy pathway between the stable and metastable forms is overlaid using green spheres, and the stable and metastable positions are indicated with orange spheres. The scale bar ranges from 0 to 58 kcal/mol.

(G) The energy plot for the minimum energy pathway between the stable and metastable forms, twisting the double bond from 180°(stable) to 10° (metastable). The blue circles indicate the minima for the stable and metastable forms. The scan coordinates are shown in Figure S35.

are 170° and 27.5° for the stable and metastable isomers, respectively, whereas flipping angles (1 2 3 4) about the naphthalene plane are −51.1° and 37.5° for the stable and metastable forms, respectively, which is an 88° *flip* of carbon 4 around the naphthalene plane. This flip can be seen in the overlay of the two phases using the naphthalene moiety as a reference (Figures 4A and S36). Photochemical isomerization of monomer **1** in solution was followed by $^{1}$H and $^{13}$C nuclear magnetic resonance (NMR), ultraviolet-visible (UV-vis) electronic absorption, Raman, and infrared (IR) spectroscopies (Figures 4B–4E, S12, and S13). Irradiation of a dilute solution of $\mathbf{1}_{st}$ in dichloromethane (DCM) at 365 nm led to a gradual bathochromic shift of the UV-vis electronic absorption spectrum (Figure 4C), which is characteristic of the photochemical formation of the metastable diastereomer $\mathbf{1}_{mst}$ via formal *E*/*Z* isomerization of the central alkene with a quantitative yield (Figure 4C, orange line). Subsequent irradiation at 455 nm resulted in partial reversion of $\mathbf{1}_{mst}$ to the stable diastereomer (Figure 4C, light blue line). Throughout both processes, isosbestic points were maintained at 385 nm, confirming a clean and unimolecular isomerization. Accordingly, characteristic shifts of $^{1}$H and $^{13}$C NMR resonances were observed in the NMR spectra of **1** in $CD_2Cl_2$ upon successive irradiation at 365 nm followed by irradiation at 455 nm, which allowed us to unambiguously identify and assign the respective diastereomers.[63] The composition of the photostationary state (PSS) established upon irradiation at both wavelengths was calculated by integration of aliphatic resonances in the $^{1}$H NMR spectrum (Figure 4B). Upon irradiation at 365 nm, a virtually complete photoconversion to the metastable diastereomer (7:93 of stable:metastable) was reached at $PSS_{365}$. In contrast, the selectivity for the reverse process was found to be modest, and at the $PSS_{455}$, a lower photoconversion (58:42 of stable:metastable) to the stable diastereomer was observed (Figure S12). In addition, the isomerization process of **1** in solution could be conveniently followed by vibrational (Raman, IR) spectroscopy (Figures 4E and S14). Raman spectra revealed a distinctive difference in the spectra of both diastereomers in the region characteristic of central alkene stretching (1,530–1,590 $cm^{-1}$) that were previously[30] demonstrated to be diagnostic for isomerization between folded stable and twisted metastable diastereomers. Similar marked changes were observed in the Fourier transform infrared (FTIR) spectra between 1,600 and 1,500 $cm^{-1}$, accompanied by prominent changes in the IR spectral region characteristic of the aliphatic C-H stretching (3,000–2,800 $cm^{-1}$), likely originating from the conformational change of the 6-membered ring associated with the isomerization (Figure S14). The photoisomerization process was further studied using DFT (see supplemental information section computational details for details) by evaluating the ground state ($S_0$) and the relevant excited states. The $S_0$ pathway shows a 32.9 kcal/mol barrier

from $\mathbf{1}_{st}$ to $\mathbf{1}_{mst}$, and the latter is 5.1 kcal/mol higher than $\mathbf{1}_{st}$, which supports thermal back-switching of the metastable to the stable diastereomer (Figures 4F and 4G). The time-dependent DFT (TD-DFT) simulated UV-vis spectra of the photoswitch core capture qualitatively the main features of the experimental UV-vis spectra (Figures 4C, S37, and S38). The simulated spectra show that only the $S_1$ and $S_2$ excited states ($S_1$—highest occupied molecular orbital (HOMO) → lowest unoccupied molecular orbital (LUMO) and $S_2$—HOMO-1 → LUMO; Figure S37) exist at wavelengths longer than 365 nm (energy excitation used) for both stable and metastable diastereomers, indicating that these two excited states can participate in the photoconversion mechanism. Irradiation at 365 nm promotes the forward conversion entering the $S_1$ and $S_2$ excited states; since the $S_1$ pathway favors back conversion, the formation of the metastable state can only occur via the $S_2$ pathway ($PSS_{365}$ = 7:93 of stable:metastable, Figures S38 and S39). Under irradiation at 455 nm, the $S_1$ (mst) pathway is selectively excited, promoting the metastable-to-stable conversion ($PSS_{455}$ = 58:42 of stable:metastable).

### Photoisomerization in the solid state

The photoisomerization behavior of the frameworks comprising bistable switch **1** was investigated with UV-vis diffuse-reflectance (DR UV-vis), Raman, DR infrared Fourier transform (DRIFT) spectroscopies, and $^{13}C$ solid-state NMR (SS NMR) (Figures 5B–5D and S21). Characteristic spectral changes were observed upon irradiation of the framework $PSF^{100}$ (for $PSF^{10}$ and $PSF^{20}$; see Figures S16, S19, S22, and S23) that, by comparison to the solution data, allowed us to unambiguously ascribe the main features due to photoswitching of monomer **1** in the solid state. In the DR UV-vis spectra of $PSF^{100}$, a large bathochromic shift was observed upon irradiation of the material at 365 nm, consistent with the reversible $\mathbf{1}_{st}$ → $\mathbf{1}_{mst}$ isomerization (Figure 5B). Additionally, a new band centered at 1,540 $cm^{-1}$ was observed in the Raman spectra of the UV-irradiated $PSF^{100}$ material, consistent with the formation of the $\mathbf{1}_{mst}$ diastereomer (Figure 5C). $^{13}C$ SS NMR spectra recorded for the irradiated material revealed upfield shifts of the aliphatic $^{13}C$ resonances ($C_a$ 35.0 ppm → 34.5 ppm and $C_c$ 29.3 ppm → 28.5 ppm), in agreement with the corresponding upfield shifts observed in solution NMR of monomer, unequivocally demonstrating photoisomerization of the OA embedded in the framework (Figure 5D; Table S4).

Notably, upon extensive irradiation of $PSF^{100}$ at 365 nm, complete photoconversion to the metastable diastereomer could be achieved as demonstrated by deconvolution of the quantitative $^{13}C$ SS NMR spectra of the bulk solid (within the accuracy of the method; Figure 5D). Similar to the monomeric $\mathbf{1}_{mst}$ dissolved in solution, the back-switching of the framework could be achieved upon irradiation of the material at 455 nm with the same moderate photoconversion to the stable diastereomer as in the solution (Figures S15 and S18). However, we observed that a significantly higher selectivity of the back-switching photoisomerization could be achieved using a longer wavelength, i.e., 505 nm as indicated by comparison of Raman and DR UV-vis (Figures 5B, 5C, S15, and S18) spectra. Indeed, quantitative analysis of the $^{13}C$ SS NMR spectra recorded for the $PSF^{100}$, irradiated at 505 nm, revealed a PSS consisting of 87% of the stable isomer: this demonstrates a much higher degree of photoconversion of the alkene in the framework compared with that achievable in solution (Figure 5D). This solid-state behavior likely originates from the bathochromic shift of the bands, compared with the monomer $\mathbf{1}_{mst}$ in solution, in the electronic absorption spectra of the photoswitch. The red-shifted spectrum of $PSF^{100}$ tails beyond 500 nm and therefore provides better spectral separation between the two diastereomers in the framework. Notably, extended (30 min) irradiation of $\mathbf{1}_{mst}$ at 505 nm in solution led to almost no photoconversion to $\mathbf{1}_{st}$ diastereomer,

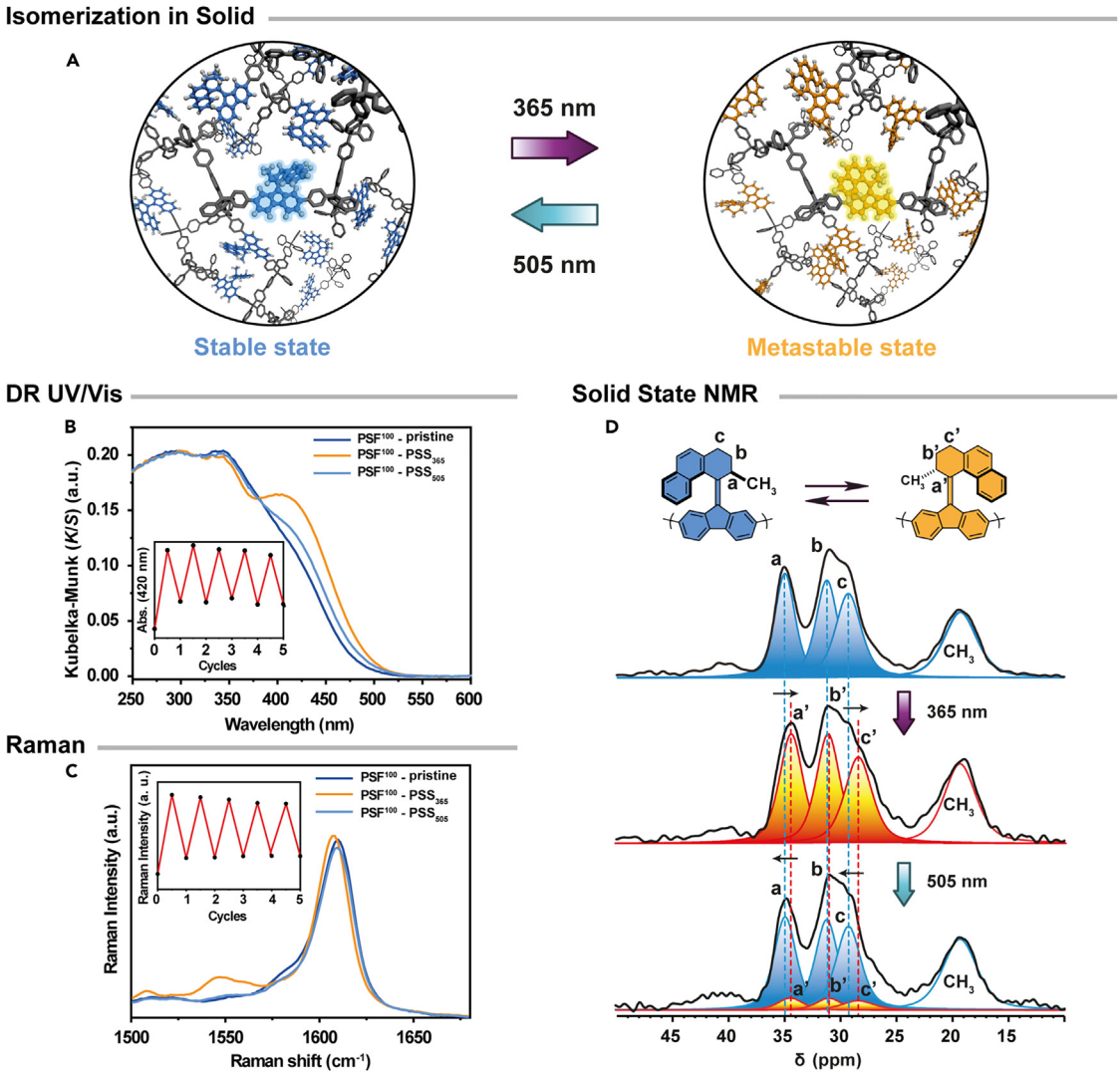


**Figure 5. Photoisomerization in the solid**

(A) Schematic representation of the photoisomerization of the $PSF^{100}$ materials.

(B) Changes in the Kubelka-Munk transformed DR UV-vis spectra of the $PSF^{100}$ material (blue spectra, $PSF^{100}$-pristine) upon irradiation at 365 nm to the photostationary state (orange spectra, $PSF^{100}$-$PSS_{365}$) and subsequent irradiation at 505 nm to regenerate the stable diastereomer (light blue spectra, $PSF^{100}$-$PSS_{505}$). The inset shows changes in the Kubelka-Munk function at 420 nm upon multiple isomerization cycles.

(C) Comparison of the baselined Raman (785 nm) spectra of the $PSF^{100}$ material (blue spectra, $PSF^{100}$-pristine) upon irradiation at 365 nm to the photostationary state (orange spectra, $PSF^{100}$-$PSS_{365}$) and subsequent irradiation at 505 nm to recover the stable diastereomer (light blue spectra, $PSF^{100}$-$PSS_{505}$). The inset shows changes in the Raman intensity at 1,550 $cm^{-1}$ upon multiple isomerization cycles.

(D) $^{13}C\{^{1}H\}$ CP-MAS solid-state NMR of a pristine $PSF^{100}$ material (top panel), after irradiation at 365 nm (middle panel) and after subsequent irradiation at 505 nm (bottom panel). See the isomerization scheme for the assignment of the $^{13}C$ resonances. Simulated blue and orange Lorentzian functions represent resonances characteristic of stable and metastable diastereomers, respectively.

indicating that this phenomenon is exclusively associated with the solid state. Additional control experiments on $PSF^{10}$ and $PSF^{20}$ frameworks revealed similar green-light responsivity for the back-switching reaction, showing no dilution dependence of this phenomenon in the system and that the photochemical behavior of the photoswitch originates from unique interactions within the aromatic framework rather than from intermolecular interactions between the photoswitches (Figure S16). The photostability studies, performed by alternating irradiation at 365/505 nm light irradiation by Raman and DR UV-vis spectroscopies, show negligible fatigue (note

the incomplete back isomerization in the first cycles), demonstrating the reversibility and robustness of the light-responsive material (Figures 5B and 5C insets). Further alternating irradiations at 365/505 nm followed by DR UV-vis spectroscopy revealed a reduction of efficiency after 15 switching cycles (Figure S40), although the photodamage is likely confined to the surface leaving the particle bulk substantially unaffected as no significant signs of fatigue in the SS NMR spectra (Figure 5D) of extensively irradiated $PSF^{100}$. In contrast, in the case of $PAF\text{-}OA^{20}$ material (see Figure 2C for structures) surface-sensitive techniques including Raman and DR UV-vis spectroscopies (Figures S17, S20, S24, and S25) showed only minor changes after irradiation at 365 nm, whereas the solid-state $^{13}C$ MAS NMR indicated no changes between the spectra of pristine sample and material irradiated at 365 nm, thus excluding any bulk photoisomerization of the switch (Figure S26). The significant constraints imposed on the photoswitches by the surrounding framework are likely restricting the photoisomerization in the bulk of the material, consequently resulting in only minor isomerization on the surface of the particles.[37]

The framework materials ($PSF^{100}$, $PSF^{20}$, and $PSF^{10}$) were subject to gas sorption experiments after irradiation at 365 nm in the solid state (Figures 6A–6E and S27; Table S5). Compared with the porosity of the pristine $PSF^{100}$ material (state I), nitrogen adsorption isotherms of the UV-irradiated $PSF^{100}$ sample collected at 77 K showed lower uptake at any partial pressure: the contraction of the accessible pore volume was evidenced in both micropore and mesopore regions (state II, 10% and 16%, respectively), as estimated from pore volume calculation according to NLDFT theory (Figures 6A and 6B; Table S5). The reversal of the phenomenon, corresponding only to the expansion of micropores (state III), was obtained by irradiation at 505 nm, showing recovery of 95% microporosity and full reversibility of the on/off switch cycle (Figures 6A and 6B, light blue). Notably, photoisomerization drives not only the configurational rearrangement of the bistable switch moiety but also a reversible reorganization of the micropore free volume, likely due to the memory of the local molecular arrangement of the pristine material.[64] This indicates the relevance of constraints to ensure that the switch conformational tension is transmitted to the local environment of the framework and expands the micropores. Conversely, in the mesopore region manifested at higher gas loading, the porosity is not entirely recovered upon irradiation at 505 nm, and the photoswitching back does not bring an efficient full recovery action because a larger conformational transmissibility through the framework is required (Figure 6D, light blue). The complete reversion to the original state of $PSF^{100}$ (state I) was successfully achieved using a chemical stimulus, i.e., by soaking in organic solvents (THF/dimethylformamide [DMF]). The porous material swelled and, after drying, reacquired its maximum absorption capacity (Figure 6C, green), exhibiting a memory effect by a solvent-assisted regeneration process. Accordingly, $PSF^{10}$ and $PSF^{20}$, with a lower content of photoswitch, show a comparable lower reduction in the pore volume upon isomerization of the photoswitches (Figures 6E and S28–S30; Table S5). In fact, by a systematic variation of the content of the two building blocks, we can widely tune the connectivity of PSFs and consequently their gas adsorption properties. These results further indicate the direct relationship between the nanoscale photo-induced photoswitch rearrangement and the bulk contraction of the framework, proving that the insertion of a large number of the photoswitching moieties constitutes an effective strategy to modulate adsorption properties (Table S5).

Importantly, in the case of a non-responsive $PAF\text{-}OA^{20}$ framework, significant changes in $N_2$ adsorption isotherms were not observed between pristine and irradiated samples (Figure 6F), strongly supporting that the observed modulation in

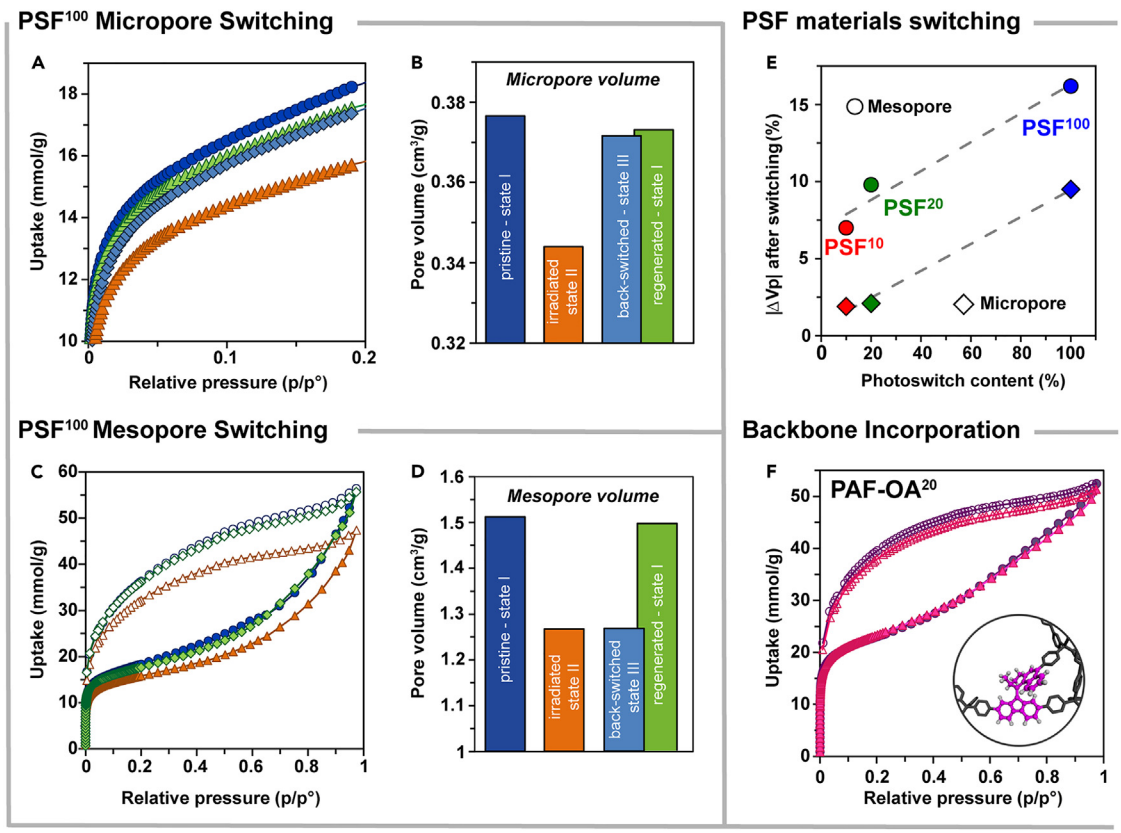


**Figure 6. Porosity switching in the solid**

(A) $N_2$ adsorption isotherms collected at 77 K and up to 0.2 p/p° of pristine $PSF^{100}$ (state I, dark blue circles), after irradiation at 365 nm (state II, orange triangles), after back optical switch by irradiation at 505 nm (state III, light blue diamonds) and solvent-assisted regeneration of $PSF^{100}$ (state I, green triangles), showing the modulation of nitrogen uptake at low partial pressures.

(B) Modulation of micropore volume related to pores with a diameter below 20 Å for $PSF^{100}$ during the irradiation cycle and solvent-assisted regeneration process.

(C) $N_2$ adsorption isotherms collected between 0 and 1 p/p° at 77 K for pristine $PSF^{100}$ (dark blue circles), after irradiation at 365 nm (orange triangles) and solvent-assisted regeneration of $PSF^{100}$ (green triangles).

(D) Calculated mesopore volume of $PSF^{100}$ over irradiation cycle and solvent-assisted regeneration process (mesoporosity between 2 and 50 nm).

(E) Decrease of the micropore and mesopore volumes of samples $PSF^{10}$, $PSF^{20}$, and $PSF^{100}$ after UV irradiation (365 nm). The absolute change in pore volume correlates with the increased amount of photoswitches in the frameworks.

(F) $N_2$ adsorption isotherms collected at 77 K of pristine $PAF\text{-}OA^{20}$ (dark purple) and after irradiation at 365 nm (pink). Inset: sketch of the framework with the bistable switch highlighting its 3-fold connectivity.

the gas adsorption capacity of $PSF^{100}$ originates exclusively from the photoisomerization of the bistable switch. In particular, this observation, along with the activation method of the material (see supplemental information of synthetic section), rules out heating of the material upon irradiation as the source of the observed performance differences, since the light-induced heat generation should be maximized in the case of a non-responsive chromophore.[58] Overall, these results highlight the paramount importance of the proper interplay of conformational freedom in a responsive network necessary to enable hierarchical amplification from the stimuli-controlled nanoscale motion to the control of the breathing of the structure. This material displays outstanding surface area and pore volume among all other photoresponsive porous materials (Table S6) and reversible bulk photoswitching behavior in the solid state, setting a benchmark for the design of photocontrolled porous solids.

### Conclusions

The design-by-purpose hexa-branched molecular-switch monomer allowed for a novel polymerization strategy, which generates a 3D poly-switch porous framework, wherein each monomer unit has an intrinsic photoswitching element. We demonstrated that the interplay of the dynamic elements, which is the bistable photoswitch and flexible backbone, systematically alternated in a robust covalent architecture realized three vastly distinct states of porosity in the framework that could be accessed in sequence upon exposure to external stimuli to produce a complete duty cycle. The large pore volume combined with a hierarchical pore structure of the photoactive material allowed full optical control over micropore contraction/expansion cycles. Consistently, contraction of the mesopores was commanded by optical stimuli, whereas full recovery to the permanent mesoporosity was assisted by solvent-swelling, regenerating the pristine material. The densely interconnected covalent network generates unique solid-state interactions that promoted unprecedented enhancement in the wavelength selectivity of bulk photochemical isomerization in the porous solid relative to the same switch in solution.

Control experiments demonstrated the relationship between the switch content and the extent of the modulation of the adsorptive properties of PSFs and highlighted the subtle interplay between the optimal degree of freedom of photoswitches and framework responsivity. Owing to the irreversible nature of the reaction, deviations from the procedure are expected to yield materials with distinct properties. Therefore, this approach is versatile and may generate a large family of materials, leading to frameworks with tailor-made properties for selected applications. These findings will facilitate the application of these materials in on-command reconfigurable gas adsorption or separation systems. In particular, the interplay of large hysteresis between adsorption and desorption branches and light-controlled size of the micropores in our material offers opportunities for the fabrication of on-demand switchable membranes for size-selective separation operating at high working capacities. In addition, further efforts dedicated to the fabrication of optically pure frameworks based on these inherent helical switches will provide opportunities to explore chiroptical switching in solid materials. In a broader context, our work illustrates that the design and synthesis of proper monomers integrating the light-responsive elements provide opportunities for the fabrication of flexible porous frameworks exhibiting new properties or states emerging from the cooperativity and intimacy between molecular functions. Future efforts aimed at engineering the intricate combination of the rigidity and flexibility of the responsive frameworks will allow harnessing and amplifying the molecular-scale motion of the light-driven artificial molecular machines more effectively and ultimately convert it into a plethora of practical outputs, similar to the operating principle of nanoscopic biological machines.[4]

## EXPERIMENTAL PROCEDURES

### Resource availability

#### *Lead contact*

Further information and requests for resources should be directed to and will be fulfilled by the lead contact, Prof. Dr. Ben L. Feringa (b.l.feringa@rug.nl).

#### *Materials availability*

All materials generated in this study are available from the lead contact upon reasonable request.

*Data and code availability*

Data related to the materials and methods, experimental procedures, and other characterization are available in the supplemental information.

## SUPPLEMENTAL INFORMATION

Supplemental information can be found online at https://doi.org/10.1016/j.chempr.2023.08.004.

## ACKNOWLEDGMENTS

This work was supported from the following sources: China Scholarship Council (CSC PhD Fellowship no. 201808330459 to J.S., no. 201707040079 to X.Z.) and China Postdoctoral Science Foundation (grant no. 2021M691003 to S.C.). We acknowledge the generous financial support from the Horizon 2020 Framework Program (ERC Advanced Investigator grant no. 694345 to B.L.F.) and the Ministry of Education, Culture, and Science of the Netherlands (Gravitation Program no. 024.001.035 to B.L.F.). The Ministero dell'Istruzione, dell'Università e della Ricerca for MIUR-Progetto Dipartimenti di Eccellenza 2018-2022, PRIN 20173L7W8K (NEMO), PRIN (SHERPA), and Lombardy Region for "Enhancing Photosynthesis" grant (2021-2023) are acknowledged for the financial support. W.D. is grateful for financial support from Marie Skłodowska-Curie Actions (Individual Fellowship no. 101027639). R. Sneep is acknowledged for mass spectral analysis. We thank Qi Zhang from the University of Groningen for fruitful discussions and Piotr Cieciórski from the University of Warsaw for the design of Figure 1.

## AUTHOR CONTRIBUTIONS

J.S., W.D., and B.L.F. conceived the project. B.L.F. and A.C. guided and supervised the research. J.S. synthesized the building blocks and all materials. J.S. carried out the UV and NMR irradiation studies in solution. X.Z. and J.S. carried out the SEM and TEM measurements. J.S. performed elemental analysis and FTIR measurements. J.S. and W.R.B. performed DR UV-vis measurments. S.C., W.D., and W.R.B. conducted Raman measurements. J.P. performed TGA, solid-state irradiation, and gas adsorption isotherms. S.K. supported sample activation and adsorption analysis. S.B. conducted solid-state irradiation and obtained SS NMR spectra. C.X.B. performed computational studies. J.S., W.D., J.P., A.C., S.B., P.S., and B.L.F. wrote the manuscript. All authors discussed the results and commented on the manuscript.

## DECLARATION OF INTERESTS

The authors declare no competing interests.

Received: April 3, 2023
Revised: June 29, 2023
Accepted: August 4, 2023
Published: August 29, 2023

## REFERENCES

1. Goulet-Hanssens, A., Eisenreich, F., and Hecht, S. (2020). Enlightening materials with photoswitches. Adv. Mater. *32*, e1905966. https://doi.org/10.1002/adma.201905966.

2. Kitagawa, S., and Uemura, K. (2005). Dynamic porous properties of coordination polymers inspired by hydrogen bonds. Chem. Soc. Rev. *34*, 109–119. https://doi.org/10.1039/B313997M.

3. He, A., Jiang, Z., Wu, Y., Hussain, H., Rawle, J., Briggs, M.E., Little, M.A., Livingston, A.G., and Cooper, A.I. (2022). A smart and responsive crystalline porous organic cage membrane with switchable pore apertures for graded molecular sieving. Nat. Mater. *21*, 463–470. https://doi.org/10.1038/s41563-021-01168-z.

4. Krause, S., and Feringa, B.L. (2020). Towards artificial molecular factories from framework-embedded molecular machines. Nat. Rev.

Chem. *4*, 550–562. https://doi.org/10.1038/s41570-020-0209-9.

5. Feng, L., Astumian, R.D., and Stoddart, J.F. (2022). Controlling dynamics in extended molecular frameworks. Nat. Rev. Chem. *6*, 705–725. https://doi.org/10.1038/s41570-022-00412-7.

6. Vukotic, V.N., Harris, K.J., Zhu, K., Schurko, R.W., and Loeb, S.J. (2012). Metal-organic frameworks with dynamic interlocked components. Nat. Chem. *4*, 456–460. https://doi.org/10.1038/nchem.1354.

7. Zhu, K., O'Keefe, C.A., Vukotic, V.N., Schurko, R.W., and Loeb, S.J. (2015). A molecular shuttle that operates inside a metal-organic framework. Nat. Chem. *7*, 514–519. https://doi.org/10.1038/nchem.2258.

8. Comotti, A., Bracco, S., and Sozzani, P. (2016). Molecular rotors built in porous materials. Acc. Chem. Res. *49*, 1701–1710. https://doi.org/10.1021/acs.accounts.6b00215.

9. Bracco, S., Miyano, T., Negroni, M., Bassanetti, I., Marchio', L., Sozzani, P., Tohnai, N., and Comotti, A. (2017). $CO_2$ regulates molecular rotor dynamics in porous materials. Chem. Commun. *53*, 7776–7779. https://doi.org/10.1039/C7CC02983G.

10. Bracco, S., Castiglioni, F., Comotti, A., Galli, S., Negroni, M., Maspero, A., and Sozzani, P. (2017). Ultrafast molecular rotors and their $CO_2$ tuning in MOFs with rod-like ligands. Chemistry *23*, 11210–11215. https://doi.org/10.1002/chem.201702930.

11. Shivanna, M., Yang, Q.Y., Bajpai, A., Patyk-Kazmierczak, E., and Zaworotko, M.J. (2018). A dynamic and multi-responsive porous flexible metal–organic material. Nat. Commun. *9*, 3080. https://doi.org/10.1038/s41467-018-05503-y.

12. Perego, J., Bracco, S., Negroni, M., Bezuidenhout, C.X., Prando, G., Carretta, P., Comotti, A., and Sozzani, P. (2020). Fast motion of molecular rotors in metal–organic framework struts at very low temperatures. Nat. Chem. *12*, 845–851. https://doi.org/10.1038/s41557-020-0495-3.

13. Perego, J., Bezuidenhout, C.X., Bracco, S., Prando, G., Marchiò, L., Negroni, M., Carretta, P., Sozzani, P., and Comotti, A. (2021). Cascade dynamics of multiple molecular rotors in a MOF: benchmark mobility at a few kelvins and dynamics control by $CO_2$. J. Am. Chem. Soc. *143*, 13082–13090. https://doi.org/10.1021/jacs.1c03801.

14. Comotti, A., Bracco, S., Ben, T., Qiu, S., and Sozzani, P. (2014). Molecular rotors in porous organic frameworks. Angew. Chem. Int. Ed. Engl. *53*, 1043–1047. https://doi.org/10.1002/anie.201309362.

15. Vogelsberg, C.S., Bracco, S., Beretta, M., Comotti, A., Sozzani, P., and Garcia-Garibay, M.A. (2012). Dynamics of molecular rotors confined in two dimensions: transition from a 2D rotational glass to a 2D rotational fluid in a periodic mesoporous organosilica. J. Phys. Chem. B *116*, 1623–1632. https://doi.org/10.1021/jp2119263.

16. Pérez-Estrada, S., Rodríguez-Molina, B., Maverick, E.F., Khan, S.I., and Garcia-Garibay, M.A. (2019). Throwing in a Monkey Wrench to Test and Determine Geared Motion in the Dynamics of a Crystalline One-Dimensional (1D) Columnar Rotor Array. J. Am. Chem. Soc. *141*, 2413–2420. https://doi.org/10.1021/jacs.8b11385.

17. Lee, J., Farha, O.K., Roberts, J., Scheidt, K.A., Nguyen, S.T., and Hupp, J.T. (2009). Metal-organic framework materials as catalysts. Chem. Soc. Rev. *38*, 1450–1459. https://doi.org/10.1039/B807080F.

18. Kreno, L.E., Leong, K., Farha, O.K., Allendorf, M., Van Duyne, R.P., and Hupp, J.T. (2012). Metal-organic framework materials as chemical sensors. Chem. Rev. *112*, 1105–1125. https://doi.org/10.1021/cr200324t.

19. Slater, A.G., and Cooper, A.I. (2015). Porous materials. Function-led design of new porous materials. Science *348*, aaa8075. https://doi.org/10.1126/science.aaa8075.

20. Hanikel, N., Prévot, M.S., and Yaghi, O.M. (2020). MOF water harvesters. Nat. Nanotechnol. *15*, 348–355. https://doi.org/10.1038/s41565-020-0673-x.

21. Feringa, B.L., and Browne, W.R. (2011). Molecular Switches (Wiley-VCH Verlag GmbH). https://doi.org/10.1002/9783527634408.

22. Pianowski, Z.L. (2022). Molecular Photoswitches (Wiley-VCH Verlag GmbH). https://doi.org/10.1002/9783527827626.

23. Browne, W.R., and Feringa, B.L. (2006). Making molecular machines work. Nat. Nanotechnol. *1*, 25–35. https://doi.org/10.1038/nnano.2006.45.

24. Balzani, V., Credi, A., and Venturi, M. (2009). Light powered molecular machines. Chem. Soc. Rev. *38*, 1542–1550. https://doi.org/10.1039/B806328C.

25. Erbas-Cakmak, S., Leigh, D.A., McTernan, C.T., and Nussbaumer, A.L. (2015). Artificial molecular machines. Chem. Rev. *115*, 10081–10206. https://doi.org/10.1021/acs.chemrev.5b00146.

26. Costil, R., Holzheimer, M., Crespi, S., Simeth, N.A., and Feringa, B.L. (2021). Directing coupled motion with light: A key step toward machine-like function. Chem. Rev. *121*, 13213–13237. https://doi.org/10.1021/acs.chemrev.1c00340.

27. Coskun, A., Banaszak, M., Astumian, R.D., Stoddart, J.F., and Grzybowski, B.A. (2012). Great expectations: can artificial molecular machines deliver on their promise? Chem. Soc. Rev. *41*, 19–30. https://doi.org/10.1039/C1CS15262A.

28. Aprahamian, I. (2020). The future of molecular machines. ACS Cent. Sci. *6*, 347–358. https://doi.org/10.1021/acscentsci.0c00064.

29. Danowski, W., Van Leeuwen, T., Browne, W.R., and Feringa, B.L. (2021). Photoresponsive porous materials. Nanoscale Adv. *3*, 24–40. https://doi.org/10.1039/D0NA00647E.

30. Castiglioni, F., Danowski, W., Perego, J., Leung, F.K.-C., Sozzani, P., Bracco, S., Wezenberg, S.J., Comotti, A., and Feringa, B.L. (2020). Modulation of porosity in a solid material enabled by bulk photoisomerization of an overcrowded alkene. Nat. Chem. *12*, 595–602. https://doi.org/10.1038/s41557-020-0493-5.

31. Chen, Q., Sun, J., Li, P., Hod, I., Moghadam, P.Z., Kean, Z.S., Snurr, R.Q., Hupp, J.T., Farha, O.K., and Fraser Stoddart, J. (2016). A redox-active bistable molecular switch mounted inside a metal-organic framework. J. Am. Chem. Soc. *138*, 14242–14245. https://doi.org/10.1021/jacs.6b09880.

32. Danowski, W., van Leeuwen, T., Abdolahzadeh, S., Roke, D., Browne, W.R., Wezenberg, S.J., and Feringa, B.L. (2019). Unidirectional rotary motion in a metal–organic framework. Nat. Nanotechnol. *14*, 488–494. https://doi.org/10.1038/s41565-019-0401-6.

33. Coudert, F.X. (2015). Responsive metal-organic frameworks and framework materials: under pressure, taking the heat, in the spotlight, with friends. Chem. Mater. *27*, 1905–1916. https://doi.org/10.1021/acs.chemmater.5b00046.

34. Castellanos, S., Kapteijn, F., and Gascon, J. (2016). Photoswitchable metal organic frameworks: turn on the lights and close the windows. CrystEngComm *18*, 4006–4012. https://doi.org/10.1039/C5CE02543E.

35. Furukawa, H., Cordova, K.E., O'Keeffe, M., and Yaghi, O.M. (2013). The chemistry and applications of metal-organic frameworks. Science *341*, 1230444. https://doi.org/10.1126/science.1230444.

36. Zhou, H.C., and Kitagawa, S. (2014). Metal-organic frameworks (MOFs). Chem. Soc. Rev. *43*, 5415–5418. https://doi.org/10.1039/C4CS90059F.

37. Krause, S., Evans, J.D., Bon, V., Crespi, S., Danowski, W., Browne, W.R., Ehrling, S., Walenszus, F., Wallacher, D., Grimm, N., et al. (2022). Cooperative light-induced breathing of soft porous crystals via azobenzene buckling. Nat. Commun. *13*, 1951. https://doi.org/10.1038/s41467-022-29149-z.

38. Diercks, C.S., and Yaghi, O.M. (2017). The atom, the molecule, and the covalent organic framework. Science *355*, eaal1585. https://doi.org/10.1126/science.aal1585.

39. Feng, X., Ding, X., and Jiang, D. (2012). Covalent organic frameworks. Chem. Soc. Rev. *41*, 6010–6022. https://doi.org/10.1039/C2CS35157A.

40. Das, G., Prakasam, T., Addicoat, M.A., Sharma, S.K., Ravaux, F., Mathew, R., Baias, M., Jagannathan, R., Olson, M.A., and Trabolsi, A. (2019). Azobenzene-equipped covalent organic framework: light-operated reservoir. J. Am. Chem. Soc. *141*, 19078–19087. https://doi.org/10.1021/jacs.9b09643.

41. Stähler, C., Grunenberg, L., Terban, M.W., Browne, W.R., Doellerer, D., Kathan, M., Etter, M., Lotsch, B.V., Feringa, B.L., and Krause, S. (2022). Light-driven molecular motors embedded in covalent organic frameworks. Chem. Sci. *13*, 8253–8264. https://doi.org/10.1039/D2SC02282F.

42. Tian, Y., and Zhu, G. (2020). Porous aromatic frameworks (PAFs). Chem. Rev. *120*, 8934–8986. https://doi.org/10.1021/acs.chemrev.9b00687.

43. Zhu, Y., and Zhang, W. (2014). Reversible tuning of pore size and $CO_2$ adsorption in azobenzene functionalized porous organic polymers. Chem. Sci. *5*, 4957–4961. https://doi.org/10.1039/C4SC02305F.

44. Brown, J.W., Henderson, B.L., Kiesz, M.D., Whalley, A.C., Morris, W., Grunder, S., Deng, H., Furukawa, H., Zink, J.I., Stoddart, J.F., et al. (2013). Photophysical pore control in an azobenzene-containing metal-organic framework. Chem. Sci. *4*, 2858–2864. https://doi.org/10.1039/C3SC21659D.

45. Kundu, P.K., Olsen, G.L., Kiss, V., and Klajn, R. (2014). Nanoporous frameworks exhibiting multiple stimuli responsiveness. Nat. Commun. *5*, 3588. https://doi.org/10.1038/ncomms4588.

46. Lyndon, R., Konstas, K., Ladewig, B.P., Southon, P.D., Kepert, P.C., and Hill, M.R. (2013). Dynamic photo-switching in metal-organic frameworks as a route to low-energy carbon dioxide capture and release. Angew. Chem. Int. Ed. Engl. *52*, 3695–3698. https://doi.org/10.1002/anie.201206359.

47. Park, J., Yuan, D., Pham, K.T., Li, J.R., Yakovenko, A., and Zhou, H.C. (2012). Reversible alteration of $CO_2$ adsorption upon photochemical or thermal treatment in a metal-organic framework. J. Am. Chem. Soc. *134*, 99–102. https://doi.org/10.1021/ja209197f.

48. Nikolayenko, V.I., Herbert, S.A., and Barbour, L.J. (2017). Reversible structural switching of a metal-organic framework by photoirradiation. Chem. Commun. *53*, 11142–11145. https://doi.org/10.1039/C7CC06074B.

49. Fan, C.B., Le Gong, L., Huang, L., Luo, F., Krishna, R., Yi, X.F., Zheng, A.M., Zhang, L., Pu, S.Z., Feng, X.F., et al. (2017). Significant enhancement of $C_2H_2/C_2H_4$ separation by a photochromic diarylethene unit: A temperature- and light-responsive separation switch. Angew. Chem. Int. Ed. Engl. *56*, 7900–7906. https://doi.org/10.1002/anie.201702484.

50. Luo, F., Fan, C.B., Luo, M.B., Wu, X.L., Zhu, Y., Pu, S.Z., Xu, W.Y., and Guo, G.C. (2014). Photoswitching $CO_2$ capture and release in a photochromic diarylethene metal-organic framework. Angew. Chem. Int. Ed. Engl. *53*, 9298–9301. https://doi.org/10.1002/anie.201311124.

51. Zheng, Y., Sato, H., Wu, P., Jeon, H.J., Matsuda, R., and Kitagawa, S. (2017). Flexible interlocked porous frameworks allow quantitative photoisomerization in a crystalline solid. Nat. Commun. *8*, 100. https://doi.org/10.1038/s41467-017-00122-5.

52. Williams, D.E., Rietman, J.A., Maier, J.M., Tan, R., Greytak, A.B., Smith, M.D., Krause, J.A., and Shustova, N.B. (2014). Energy transfer on demand: photoswitch-directed behavior of metal-porphyrin frameworks. J. Am. Chem. Soc. *136*, 11886–11889. https://doi.org/10.1021/ja505589d.

53. Furlong, B.J., and Katz, M.J. (2017). Bistable dithienylethene-based metal-organic framework illustrating optically induced changes in chemical separations. J. Am. Chem. Soc. *139*, 13280–13283. https://doi.org/10.1021/jacs.7b07856.

54. Williams, D.E., Martin, C.R., Dolgopolova, E.A., Swifton, A., Godfrey, D.C., Ejegbavwo, O.A., Pellechia, P.J., Smith, M.D., and Shustova, N.B. (2018). Flipping the switch: fast photoisomerization in a confined environment. J. Am. Chem. Soc. *140*, 7611–7622. https://doi.org/10.1021/jacs.8b02994.

55. Dolgopolova, E.A., Galitskiy, V.A., Martin, C.R., Gregory, H.N., Yarbrough, B.J., Rice, A.M., Berseneva, A.A., Ejegbavwo, O.A., Stephenson, K.S., Kittikhunnatham, P., et al. (2019). Connecting wires: photoinduced electronic structure modulation in metal-organic frameworks. J. Am. Chem. Soc. *141*, 5350–5358. https://doi.org/10.1021/jacs.8b13853.

56. Baroncini, M., d'Agostino, S., Bergamini, G., Ceroni, P., Comotti, A., Sozzani, P., Bassanetti, I., Grepioni, F., Hernandez, T.M., Silvi, S., et al. (2015). Photoinduced reversible switching of porosity in molecular crystals based on star-shaped azobenzene tetramers. Nat. Chem. *7*, 634–640. https://doi.org/10.1038/nchem.2304.

57. Wang, Z., Müller, K., Valášek, M., Grosjean, S., Bräse, S., Wöll, C., Mayor, M., and Heinke, L. (2018). Series of photoswitchable azobenzene-containing metal-organic frameworks with variable adsorption switching effect. J. Phys. Chem. C *122*, 19044–19050. https://doi.org/10.1021/acs.jpcc.8b05843.

58. Castellanos, S., Goulet-Hanssens, A., Zhao, F., Dikhtiarenko, A., Pustovarenko, A., Hecht, S., Gascon, J., Kapteijn, F., and Bléger, D. (2016). Structural effects in visible-light-responsive metal-organic frameworks incorporating Ortho-Fluoroazobenzenes. Chemistry *22*, 746–752. https://doi.org/10.1002/chem.201503503.

59. Wang, Z., Knebel, A., Grosjean, S., Wagner, D., Bräse, S., Wöll, C., Caro, J., and Heinke, L. (2016). Tunable molecular separation by nanoporous membranes. Nat. Commun. *7*, 13872. https://doi.org/10.1038/ncomms13872.

60. Pooler, D.R.S., Lubbe, A.S., Crespi, S., and Feringa, B.L. (2021). Designing light-driven rotary molecular motors. Chem. Sci. *12*, 14964–14986. https://doi.org/10.1039/D1SC04781G.

61. Perego, J., Piga, D., Bracco, S., Sozzani, P., and Comotti, A. (2018). Expandable porous organic frameworks with built-in amino and hydroxyl functions for $CO_2$ and $CH_4$ capture. Chem. Commun. *54*, 9321–9324. https://doi.org/10.1039/C8CC03951H.

62. Ben, T., Ren, H., Ma, S., Cao, D., Lan, J., Jing, X., Wang, W., Xu, J., Deng, F., Simmons, J.M., et al. (2009). Targeted synthesis of a porous aromatic framework with high stability and exceptionally high surface area. Angew. Chem. Int. Ed. Engl. *48*, 9457–9460. https://doi.org/10.1002/anie.200904637.

63. Sheng, J., Danowski, W., Crespi, S., Guinart, A., Chen, X., Stähler, C., and Feringa, B.L. (2023). Designing P-type bi-stable overcrowded alkene-based chiroptical photoswitches. Chem. Sci. *14*, 4328–4336. https://doi.org/10.1039/D2SC05903G.

64. Rozyyev, V., Thirion, D., Ullah, R., Lee, J., Jung, M., Oh, H., Atilhan, M., and Yavuz, C.T. (2019). High-capacity methane storage in flexible alkane-linked porous aromatic network polymers. Nat. Energy *4*, 604–611. https://doi.org/10.1038/s41560-019-0427-x.